Nanoscale

Accepted Manuscript

This article can be cited before page numbers have been issued, to do this please use: S. Kwon, W. Lee, R. Aymerich Armengol, Y. M. Jung, S. Hwang, C. Scheu and J. Lim, *Nanoscale*, 2026, DOI: 10.1039/D6NR00179C.

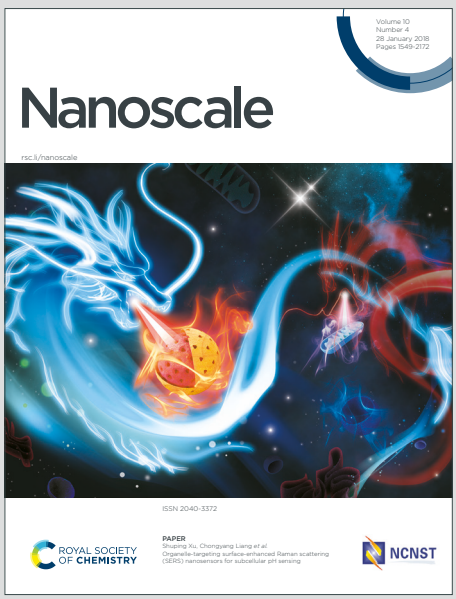

ROYAL SOCIETY OF CHEMISTRY

rsc.li/nanoscale

View Article Online
DOI: 10.1039/D6NR00179C

ARTICLE

Bottom-up sol-gel synthesis of 2D lead glycolate and oxide nanostructures towards electrochemical ozone production

Received 00th January 20xx,
Accepted 00th January 20xx

DOI: 10.1039/x0xx00000x

Soohyun Kwon, ‡[a] Woojin Lee, ‡[a] Raquel Aymerich Armengol, [b] Young Mee Jung, [c] Seong-Ju Hwang, [d] Christina Scheu, [e] and Joohyun Lim* [a]

Despite extensive progress on two-dimensional (2D) materials, 2D lead oxides remain underexplored, limiting systematic structure–property studies. Here, we develop a bottom-up sol-gel synthesis route to 2D lead glycolate (PG) and oxide nanostructures via finely tuned hydrolysis–condensation of molecular metal alkoxides. The hydrolysis–condensation in ethylene glycol (EG), with controlled Pb-EG precursor/water and water/alcohol ratios, yields 2D-assembled nanoparticles, elongated nanostructures, and single-crystalline 2D hexagonal nanoplates. While calcination at 450 °C leads to a conversion of PG to tetragonal Pb_3O_4 with a significant collapse of 2D morphology, the introduction of a SiO_2 overlayer can preserve the original 2D architecture of PG, affording 2D-assembled Pb_3O_4/SiO_2 with minimal aggregation. The higher overpotential of 2D-assembled Pb_3O_4/SiO_2, with a delayed current-onset potential, evidences its enhanced selectivity for electrochemical ozone production over oxygen evolution. This is further confirmed by a higher current density and a smaller Tafel slope in the high-potential region above ~2.8 V. KI–starch assay and UV–Vis spectroscopy confirm more efficient ozone generation by 2D-assembled Pb_3O_4/SiO_2 compared to aggregated Pb_3O_4. This morphology-preserving route offers a general strategy for synthesizing structurally defined 2D lead oxide catalysts with enhanced performance.

Introduction

Molecular metal alkoxides have been used as standard precursors for synthesizing metal oxide materials via the sol-gel method.[1,2] Both inorganic metal centers and organic alkoxide ligands contribute significantly to the nanomaterial synthesis. In particular, transition metals with partially filled d- or f-orbitals readily form metal alkoxides due to their high coordination ability. Organic ligands, such as polyalcohols and aromatic alcohols, can guide the solid-state metal alkoxides formation through bridging oxygen atoms or π–π interactions between phenyl groups. Solid-state metal alkoxides derived in this way have attracted growing attention as precursors or templates for tailoring nanomaterial morphologies.[2] Building on this interest, they have been utilized as stable precursors to synthesize functional metal oxides for photocatalysts, battery electrodes, gas sensors, etc.[3,4] Despite the broad potential of metal alkoxides, especially in controlling shape and dimension, their application to lead-based materials remains unexplored. One rare example is the work by Xia et al., where lead glycolate nanowires served as precursors for PbO nanoparticles interconnected in a wire-like structure.[5] Moreover, although two-dimensional (2D) nanostructures possess unique physicochemical advantages, their direct formation from lead-based alkoxides has not been fully realized.[6]

2D nanostructures, such as nanosheets and nanoplates, are of great interest due to their high anisotropy and thin thickness, leading to tunable band gaps, nonlinear optical properties, and high stability.[6–8] Traditional fabrication of 2D nanostructures often relies on top-down approaches like mechanical or chemical exfoliation from bulk layered crystal structures. However, bottom-up synthetic strategies, particularly those employing molecular precursors or guided assembly, offer alternative and potentially more versatile routes to such nanostructures.[9]

For lead oxides, 2D nanostructures have been produced through the exfoliation of layered crystal structures of α- and β-PbO.[8,10] Electrodeposition and laser ablation have also been employed to obtain 2D PbO nanosheets.[8,11,12] In addition, other 2D lead-based materials, such as $2PbCO_3{\cdot}Pb(OH)_2$, have been synthesized using precipitation methods.[13] However, highly crystalline 2D lead-based nanostructures prepared via bottom-up strategies remain rarely reported, and a comprehensive synthetic framework is still lacking.

[a] Department of Chemistry, Institute for Molecular Science and Fusion Technology, Multidimensional Genomics Research Center
Kangwon National University
Chuncheon, Gangwon 24341, Republic of Korea
E-mail: jlim@kangwon.ac.kr
[b] Center for Visualizing Catalytic Processes
Technical University of Denmark
2800 Kongens Lyngby, Denmark
[c] Department of Chemistry, Institute for Molecular Science and Fusion Technology
Kangwon National University
Chuncheon, Gangwon 24341 Republic of Korea.
[d] Department of Materials Science and Engineering, College of Engineering
Yonsei University
Seoul 03722, Republic of Korea
[e] Max-Planck-Institut für Nachhaltige Materialien GmbH
Max-Planck-Straße 1, Düsseldorf 40237, Germany
‡ These authors contributed equally to this work

Lead oxides are intrinsically crucial in industrial fields such as batteries, pigments, paints, and petrochemical processes.[14] They have recently been recognized as promising catalysts for oxidative water purification and electrochemical ozone production (EOP).[15] Although the size, facet, and morphology have been tuned to optimize EOP properties, studies applying 2D structures to lead oxide for EOP have been scarcely reported.[16–21] Accordingly, to obtain the unique properties of 2D lead oxides, including catalysis, energy storage, sensors, and optoelectronics, developing new synthetic approaches to such materials is of significant interest.[22]

In this work, we report a novel bottom-up synthesis of lead-glycolate (PG) structures, including 2D-assembled nanoparticles, 2D-elongated nanostructures, and well-defined 2D hexagonal nanoplates (Scheme 1). Ethylene glycol (EG) was used as both a solvent and a coordinating ligand, guiding the formation of 2D structures through glycolate complexation. By tuning the relative ratios of the precursor and solvent, various 2D morphologies were obtained. Among them, the 2D-assembled PG nanoparticles were then converted into crystalline Pb_3O_4 while preserving their 2D morphologies, enabled by a SiO_2 overlayer. Finally, the resulting 2D Pb_3O_4 nanostructures were evaluated as EOP electrocatalysts with optimized selectivity. This highlights the potential of the synthetic platform for practical applications.

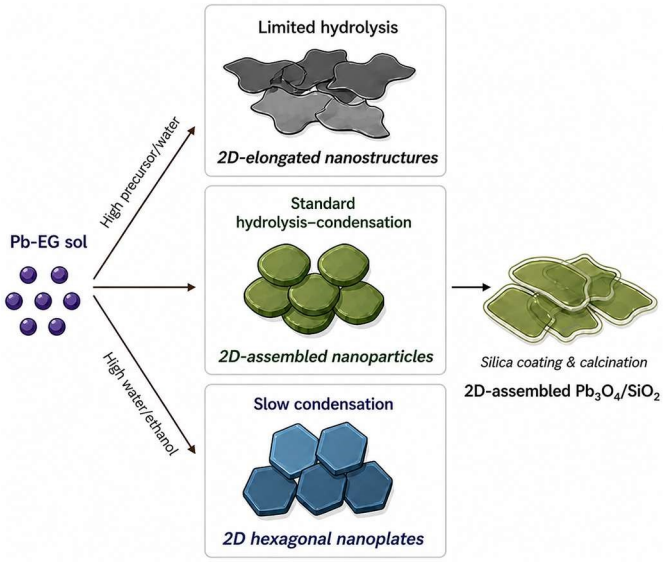

Scheme 1. Synthetic route of 2D lead glycolate and oxide nanostructures.

Experimental section

Materials

Lead acetate trihydrate (≥99%), ethylene glycol (≥99%), and acetone (99.5%) were purchased from Sigma-Aldrich. Ethanol (99.9%), methanol (99.8%), 1-propanol (99.5%), and ammonia solution (25.0~30.0% and 28.0~30.0%) were purchased from Samchun. Tetraethyl orthosilicate (TEOS, >98.0%) was purchased from Tokyo Chemical Industry. 1-Butanol (99%), sodium sulfate (Na_2SO_4, 99%), potassium iodide (KI, 99%), and starch were purchased from Thermo Scientific. Nafion solution (5 wt%) and carbon paper with MPL (MPL-CP, GDL210S, CeTech) were obtained from Nara Cell-Tech. Deionized water purified with the AquaMAX system was used.

Synthesis of 2D-assembled PG nanostructures using water

Lead acetate trihydrate (56 mg) was dissolved in EG (10 mL) and stirred for 8 hours. Pb-EG precursor solution (1 mL) was then injected into a mixed solution of water (1 mL) and ethanol (11 mL) under stirring (400 rpm), and the reaction proceeded for 2 hours. The resulting product was collected by centrifugation and washed several times with ethanol.

The total reaction volume was maintained at 13 mL, and the relative proportions of the precursor solution, water, and ethanol were systematically modulated. For the experiments examining the effect of the precursor-to-water ratio, the total reaction volume was allowed to vary. Unless otherwise stated, these parameters were used as the standard reaction condition (precursor : water : ethanol volume ratio = 1 : 1 : 11).

Synthesis of 2D-assembled PG nanoparticles using ammonia

Lead acetate trihydrate (112 mg) was dissolved in EG (20 mL) and stirred for 8 hours. Pb-EG precursor solution (20 mL) was then injected into a mixed solution of ethanol (220 mL) and ammonia solution (25.0~30.0%, 20 mL) under stirring (400 rpm), and the reaction proceeded for 2 hours. The resulting white product was collected by centrifugation and washed several times with ethanol.

Synthesis of silica-coated 2D-assembled PG nanoparticles and 2D-assembled Pb_3O_4/SiO_2

TEOS (10 μL) was dissolved in ethanol (10 mL). The resulting TEOS solution was added to the 2D-assembled PG nanoparticle solution (20 mg/3.5 mL). Ammonia solution (28.0~30.0%, 0.4 mL) was then introduced under continuous stirring (400 rpm), and the reaction proceeded for 6 hours. An additional TEOS solution (0.5 mL) was injected at 2 and 4 hours. The resulting product was collected by centrifugation, washed several times with ethanol, and dried. The obtained powder was calcined at 450 °C (2 °C min^{-1}) for 12 hours under an oxygen flow (100 mL min^{-1}).

Characterizations

The morphology and elemental composition of 2D PG-based nanostructures were characterized using scanning electron microscopy (SEM; S-4800, Hitachi, 15 kV and Quattro ESEM, Thermo Fisher, 20 kV) and transmission electron microscopy (TEM; JEM-2100F, JEOL, 200 kV and Tecnai G2 F30, FEI, 300 kV) equipped with an energy-dispersive X-ray spectroscopy (EDS; AZtec, Oxford Instruments and XFlash 7, Bruker) detector. High-resolution imaging and elemental mapping were conducted with probe-corrected scanning TEM (STEM; Spectra Ultra STEM, Thermo Fisher, 300 kV) equipped with an Ultra-X EDS detector. Atomic force microscopy (AFM; NX10, Park Systems) was used to measure the thickness of nanostructures. Thermogravimetric

analysis (TGA; SDT650, TA Instruments) was performed to confirm the glycolate content. Powder X-ray diffraction (XRD; Miniflex 600, Rigaku) with Cu Kα radiation was employed to analyze the crystal structure. Fourier transform infrared (FT-IR; iS50, Thermo Fisher) spectroscopy was utilized to examine the bonding structure. To analyze the phase, Raman spectroscopy (LabRAM HR, Horiba) with a 785 nm laser was conducted. The band gap was investigated by ultraviolet-visible (UV-Vis; V-770, Jasco) diffuse reflectance spectroscopy. X-ray photoelectron spectroscopy (XPS; PHI 5000 VersaProbe, Ulvac-PHI) with Al Kα radiation was performed to characterize the oxidation state.

Electrode preparation

MPL–CP electrode (1 × 1.2 cm^2) was cleaned with water, acetone, and ethanol, and then dried. The catalyst (2.4 mg) and Nafion solution (30 µL) were dispersed in an ethanol–water mixture (1:1 v/v, 270 µL) by sonication for 30 minutes. The resulting ink was drop-cast onto the MPL–CP electrode (loading 2 mg cm^{-2}) and then dried in a vacuum oven at 60 °C for 24 hours.

Electrochemical measurements

All electrochemical analyses were performed in 0.2 M Na_2SO_4 using a three-electrode system controlled by a potentiostat (ZIVE MP2F, WonATech). The catalyst-loaded MPL–CP electrode connected with copper tape served as the working electrode, while an Ag/AgCl (in saturated KCl) and a Pt mesh with wire were used as the reference and counter electrodes, respectively. Linear sweep voltammetry (LSV) was performed in the potential range of 0 to 3 V vs. Ag/AgCl at a scan rate of 5 mV s^{-1}. And the electrochemical surface area (ECSA) was estimated from the double-layer capacitance (C_{dl}) by cyclic voltammetry (CV) in the potential range of 0.6 to 1.2 V vs. Ag/AgCl at different scan rates from 20 to 100 mV s^{-1}. All potentials were calibrated against the reversible hydrogen electrode (RHE) according to the Nernst equation:

$$E(RHE) = E(Ag/AgCl) + 0.059 \times pH + 0.197\ V$$

Ozone quantification

The iodine–starch method was employed to quantify the amount of dissolved ozone. To obtain the ozone-containing electrolyte, chronopotentiometry was conducted in 50 mL of electrolyte at constant current densities of 30, 60, and 90 mA cm^{-2} for 20 minutes. After the reaction, 10 mL of the electrolyte was mixed with 5 mL of KI solution (20 wt%) and stirred until the yellow color stabilized. Then, 1 mL of starch solution (2 wt%) was added, resulting in a blue color. The color intensity, corresponding to ozone concentration, was tested by UV–Vis spectroscopy (V-770, Jasco).

Results and discussion

Controlled synthesis of 2D lead glycolate nanostructures

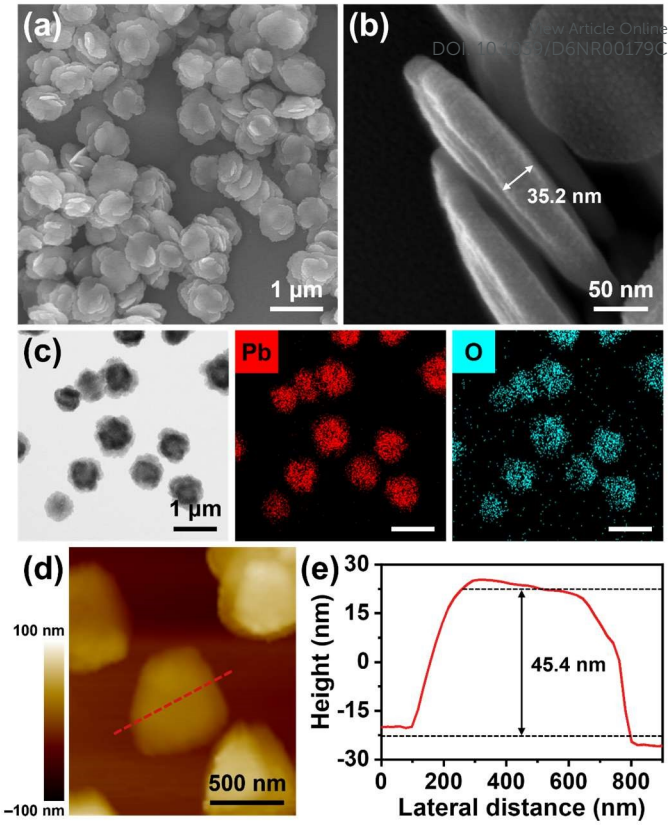

Fig. 1 (a, b) SEM images, (c) TEM image with EDS elemental maps, (d) AFM image, and (e) height profile of 2D-assembled PG nanoparticles.

2D PG nanostructures were synthesized through a sol-gel reaction in an ethanol solvent, using lead acetate, EG, and water. In this process, Pb-EG complexes were hydrolyzed by water and condensed to form nanostructures, following the typical hydrolysis–condensation mechanism of metal alkoxides.[23,24] SEM images showed that the as-prepared PG nanoparticles (~600 nm) consist of aggregated 2D sub-nanostructures with a thickness of ~35 nm (Fig. 1a and b). TEM image and EDS maps obtained in TEM revealed their 2D assembly and homogeneous distribution of Pb and O (Fig. 1c). AFM analysis measured particle heights of ~45 nm (Fig. 1d and e), while some particles exhibited heights from ~45 to 58 nm (Fig. S1). This indicates that a few 2D sub-nanostructures of ~20 to 30 nm, as confirmed by SEM images, are assembled into a nanoparticle, resulting in a final thickness of ~40 to 60 nm. No particles were synthesized without using water (Fig. S2a and b), confirming the essential role of water in hydrolysis–condensation synthesis.

The relative water amount was tuned by varying the Pb-EG precursor-to-water ratio. Higher Pb-EG precursor content at low amount of water yielded 2D-elongated sub-nanostructures that interconnected on the micrometer scale (Fig. 2). This result is reminiscent of pH-dependent silica growth, where slower condensation in acidic conditions leads to more extended structures.[25,26] However, in our case, when increasing the Pb-EG content under water-limited conditions, hydrolysis becomes increasingly restricted, thereby favoring less-dense, elongated assemblies rather than well-defined particles. In this way, the

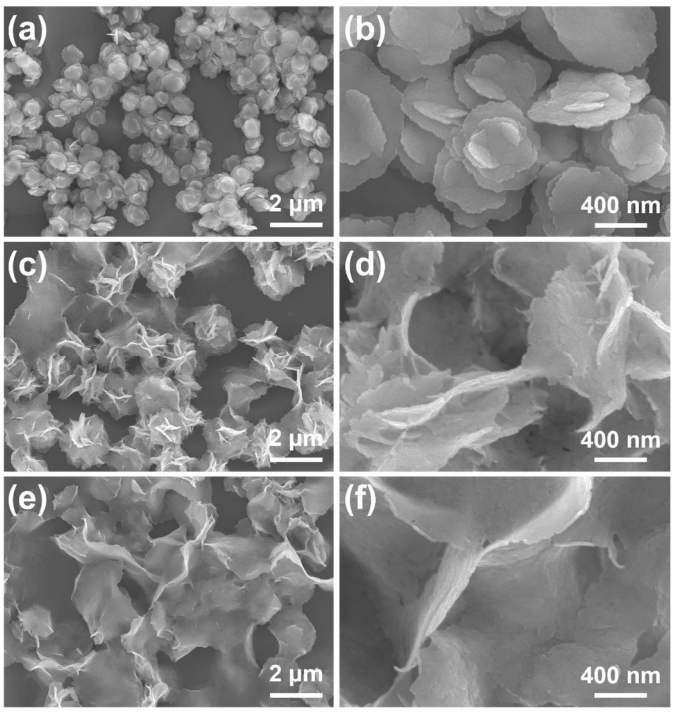

Fig. 2 SEM images of PG nanostructures synthesized with increasing precursor-to-water ratio at constant ethanol contents, resulting in 2D-elongated morphologies. The precursor : water : ethanol volume ratios are (a, b) 0.1 : 0.1 : 12, (c, d) 0.5 : 0.1 : 12, and (e, f) 1.0 : 0.1 : 12.

Pb-EG precursor seems to play as a structure-directing agent in forming the 2D morphology.

To investigate solvent effects, the synthesis was conducted in various solvents. Using water as the main solvent resulted in rarely observed enlarged hexagonal particles (Fig. S2c), while

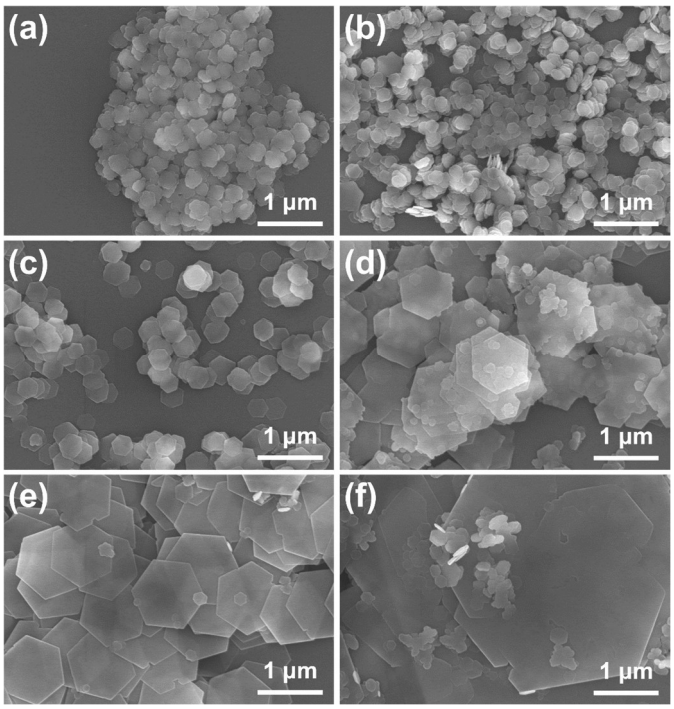

Fig. 3 SEM images of PG nanostructures synthesized with increasing water-to-ethanol ratio at constant precursor content, resulting in 2D hexagonal nanoplates. The precursor : water : ethanol volume ratios are (a) 1 : 1 : 11, (b) 1 : 3 : 9, (c) 1 : 5 : 7, (d) 1 : 7 : 5, (e) 1 : 9 : 3, and (f) 1 : 11 : 1.

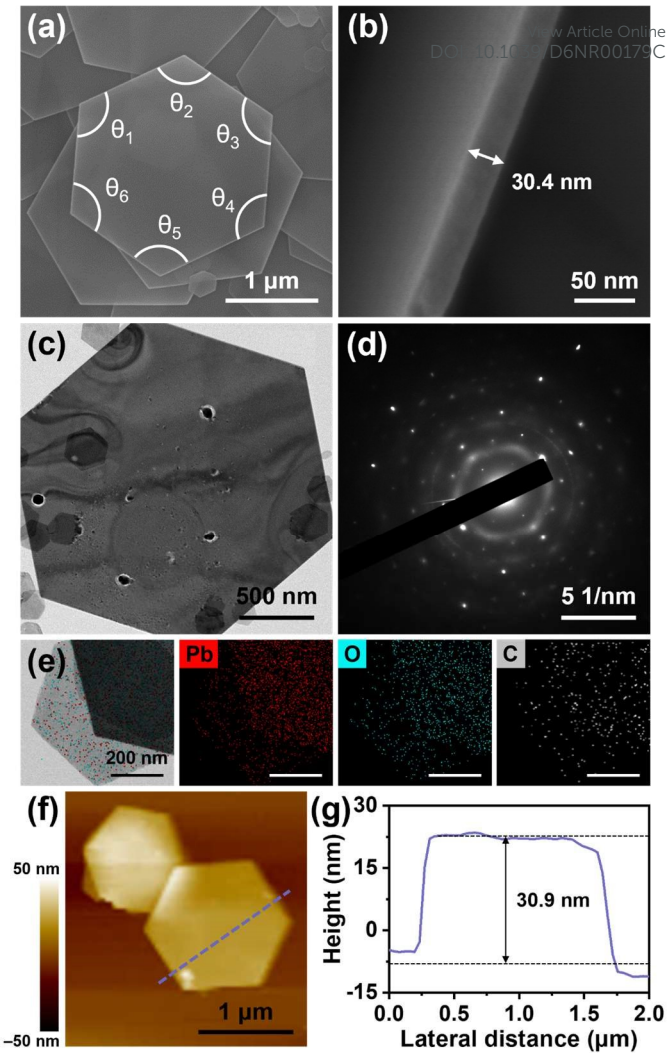

Fig. 4 (a, b) SEM images, (c) TEM image, (d) SAED pattern, (e) TEM-EDS elemental maps, (f) AFM image, and (g) height profile of 2D hexagonal nanoplates.

acetone produced highly aggregated precipitates (Fig. S2d). According to previous reports, the Ti-EG precursor solution formed spherical Ti-glycolate nanoparticles only in acetone or similar solvents containing a ketone group, like cyclohexanone, 1,4-dioxane, and tetrahydrofuran. While these solvents all feature an oxygen atom with two lone-pair electrons, the exact reason remains unclear.[23,24] Each transition metal-glycolate precursor appears to require a specific hydrolysis–condensation rate and solubility, determined by the solvent, to achieve individual nanoscale precipitation with high yield. In addition, when alcohols such as methanol, 1-propanol, and 1-butanol were used as solvents, colloidal 2D PG nanoparticles formed (Fig. S3). Particle sizes were comparable when the alcohol solvent had a longer alkyl chain than ethanol. In contrast, larger-sized 2D-assembled PG nanoparticles were obtained in methanol solvent, which has a shorter alkyl chain than ethanol. This suggests that faster condensation in methanol solvent induces the formation of numerous small seeds that tend to aggregate during growth, similar to the well-known mechanism of silica nanoparticle formation.[27,28] This is further supported by the

formation of larger, aggregated particles when the Pb concentration was increased by ten times in ethanol (Fig. S4).

Such profound roles of water and ethanol in our standard reaction conditions enable precise tuning of the 2D morphology of PG nanostructures. Systematic variation of the ethanol-to-water ratio from 11:1 to 1:11 revealed that increasing relative water content promoted the formation of well-defined 2D hexagonal PG nanoplates up to ~6 μm (Fig. 3). Higher relative water content slows the condensation rate, providing sufficient time to achieve thermodynamically driven, oriented growth into faceted 2D nanostructures.

The hexagonal plates displayed interior angles of 119~120° for $\theta_{1\sim6}$, consistent with a perfect hexagonal symmetry structure (Fig. 4a). The vertical SEM image in Fig. 4b revealed their thickness of ~30 nm, while the TEM image confirmed their thin thickness through transparency (Fig. 4c). Selected area electron diffraction (SAED) showed spot patterns from a big 2D hexagonal PG nanoplate, indicating a single-crystalline nature (Fig. 4d). EDS elemental maps showed that 2D hexagonal PG nanoplates are homogeneously composed of Pb, O, and C (Fig. 4e). AFM image presents a 2D hexagonal PG nanoplate with a thickness of ~30 nm (Fig. 4f and g).

Lead oxide conversion and electrocatalytic performance

Among the morphologies synthesized above, 2D-assembled PG nanoparticles were chosen for further studies due to their high synthesis yield. To increase the amount of 2D-assembled PG nanoparticles for characterizations and application, ammonia served as a basic catalyst to enhance the condensation reaction. The obtained 2D-assembled PG nanoparticles exhibited similar 2D morphology (Fig. S5). As shown in the TGA plot (Fig. 5a), ~2.5 wt% weight loss occurred below 200 °C due to water desorption, followed by an additional ~15.0 wt% loss at higher temperature due to glycolate removal. Also, powder XRD pattern showed a characteristic peak at ~10°, typical of metal glycolates stacked from chain-like complexes (Fig. 5b).[5,29] FT-IR spectrum exhibited distinct peaks at 1045 and 579 cm^{-1}, corresponding to the C–O–Pb and O–Pb stretching modes, respectively, confirming the coordination between Pb center and glycolate ligand (Fig. S6).[30,31] As a result, these support the pivotal role of bidentate glycolate ligands in stabilizing Pb coordination and directing 2D assembly.

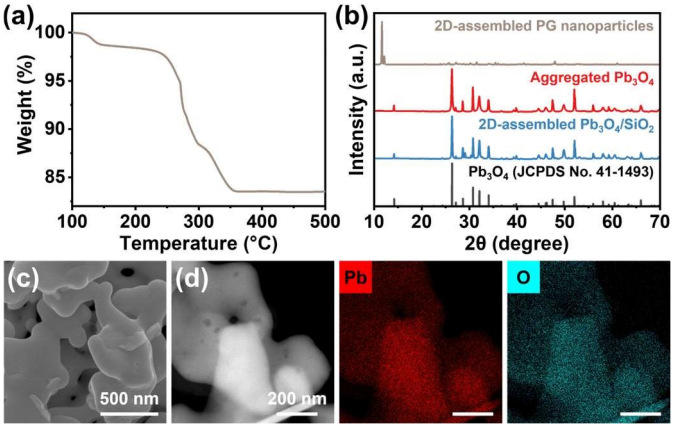

Fig. 5 (a) TGA plot of 2D-assembled PG nanoparticles. (b) XRD patterns of 2D-assembled PG nanoparticles, aggregated Pb_3O_4, and 2D-assembled Pb_3O_4/SiO_2. (c) SEM image and (d) HAADF-STEM image with EDS elemental maps of aggregated Pb_3O_4.

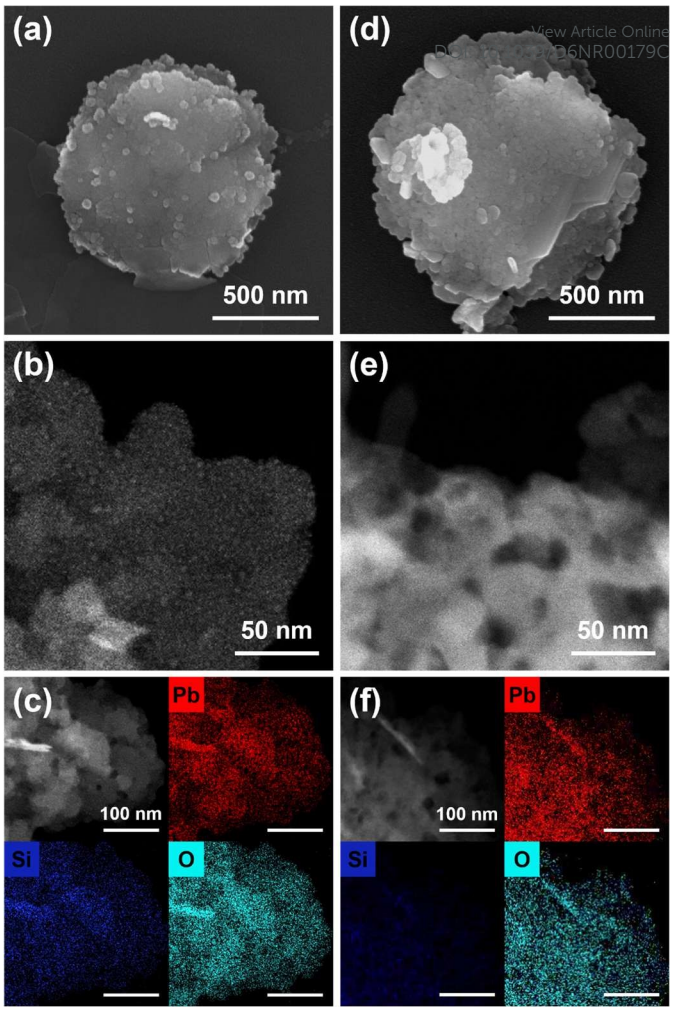

Fig. 6 (a) SEM image, (b) HAADF-STEM image, and (c) EDS elemental maps of silica-coated 2D-assembled PG nanoparticles. (d) SEM image, (e) HAADF-STEM image, and (f) EDS elemental maps of 2D-assembled Pb_3O_4/SiO_2.

To prepare 2D lead oxide catalysts for EOP, 2D-assembled PG nanoparticles were calcined at 450 °C under an oxygen flow. Powder XRD patterns after calcination showed intense (110), (211), and (202) reflections, characteristic of tetragonal Pb_3O_4 (Fig. 5b).[32,33] However, during calcination, the original 2D morphology collapsed, resulting in larger crystalline Pb_3O_4 aggregates (Fig. 5c–d). To prevent this agglomeration, a SiO_2 overlayer was applied before calcination. The introduced metal oxide coating layer, including silica, could be advantageous for achieving EOP catalysts with higher overpotentials, which are crucial for enhancing EOP selectivity over oxygen evolution reaction (OER).[20,34] Silica-coated 2D-assembled PG nanoparticles are displayed in the SEM image of Fig. 6a. High-angle annular dark field STEM (HAADF-STEM) image shows the silica coating of 2D-assembled PG nanoparticles by bright dots (Fig. 6b). The homogeneous silica coating was confirmed by EDS elemental maps of Pb, Si, and O (Fig. 6c). After calcination, silica-coated 2D-assembled PG nanoparticles retained their 2D morphology, yielding 2D-assembled Pb_3O_4/SiO_2 with minimal

View Article Online
DOI: 10.1039/D6NR00479C

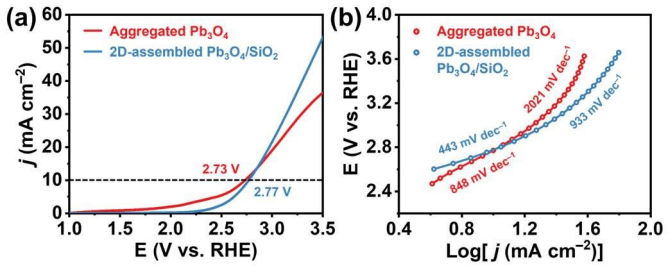

Fig. 7 (a) LSV curves and (b) Tafel plots of aggregated Pb_3O_4 and 2D-assembled Pb_3O_4/SiO_2.

aggregation (Fig. 6d–f). Furthermore, the crystallite sizes were calculated using the Scherrer equation for multiple diffraction planes, indicating no significant difference between aggregated Pb_3O_4 and 2D-assembled Pb_3O_4/SiO_2 (Table S1). FT-IR spectra of the calcined samples showed the O–Pb stretching band at ~530 cm^{-1}, along with vibrational bands from water adsorbed on the pellet (Fig. S6).[5,35] The only observable difference is additional vibrational bands from a SiO_2 overlayer. Raman spectra of both samples showed characteristic bands of Pb_3O_4 at ~121, ~390, and ~550 cm^{-1}, consistent with the XRD patterns, confirming that Pb_3O_4 is the dominant phase after calcination, regardless of the presence of a SiO_2 overlayer (Fig. 5b and S7).[36] Moreover, the band gaps of both samples were found to be nearly identical (Fig. S8). As shown in Fig. S9, the presence of a trace amount of β-PbO in 2D-assembled Pb_3O_4/SiO_2 likely results from limited oxidation induced by the silica coating, which is in agreement with the slightly lower Pb^{4+}/Pb^{2+} ratio observed in XPS (Fig. S10).

To examine the influence of 2D structure on EOP activity, LSV was conducted on aggregated Pb_3O_4 and 2D-assembled Pb_3O_4/SiO_2 in a 0.2 M Na_2SO_4 electrolyte. As shown in Fig. 7a, 2D-assembled Pb_3O_4/SiO_2 showed a higher overpotential of ~2.77 V than ~2.73 V of aggregated Pb_3O_4 at 10 mA cm^{-2}. Besides, aggregated Pb_3O_4 displays an earlier onset potential, implying stronger OER contributions that compete with EOP. Above ~2.85 V, 2D-assembled Pb_3O_4/SiO_2 delivered a higher current density, indicating a larger ozone production. These overall LSV trends remained consistent. And their overpotential is comparable to that of lead oxide-based EOP catalysts (Table S2). Tafel plots further support this result (Fig. 7b). 2D-assembled Pb_3O_4/SiO_2 showed smaller slopes of 443 and 933 mV dec^{-1} in the low- and high-current regions, compared with 848 and 2021 mV dec^{-1} for aggregated Pb_3O_4. According to previous reports, the low-current region was dominated by OER, while the high-current region involves both OER and EOP.[37,38] Yet, the interpretations of Tafel slopes vary. Some studies linked a higher Tafel slope in the high-current region to suppressed OER and enhanced EOP, whereas others argued that a smaller Tafel slope reflects a lower activation energy barrier, which is favorable to the 6-electron EOP path.[38–40] In our case, the later onset potential (indicating suppressed OER), the higher current density in the high-potential region, and the smaller Tafel slope all point toward improved EOP selectivity of 2D-assembled Pb_3O_4/SiO_2. Furthermore, as shown in Fig. R11, its lower ECSA indicates that the enhanced activity is determined more by selectivity than by surface area. To compare ozone generation directly, the ozone produced after electrocatalytic reactions at current densities of 30 to 90 mA cm^{-2} was quantified using the KI–starch method. As current density increased, the color of the electrolyte with the KI solution (yellow) and the subsequent starch–iodine complex (violet) became more intense, reflecting a higher amount of ozone produced (Fig. S12a–d). At low current densities (30 and 60 mA cm^{-2}), both catalysts exhibited similar UV-Vis absorbance due to the primarily dominant OER (Fig.S12e and f). In contrast, at high current densities (90 mA cm^{-2}), where both OER and EOP occur, a significant increase in ozone generation was observed for 2D-assembled Pb_3O_4/SiO_2, indicating higher EOP selectivity compared to aggregated Pb_3O_4.

The enhanced EOP selectivity of 2D-assembled Pb_3O_4/SiO_2 is likely associated with the 2D morphology-preserved lead oxide and SiO_2 interface rather than other structural factors. The SiO_2 overlayer can suppress severe aggregation during calcination and may partially regulate the accessibility of water molecules to OER-favorable sites, thereby delaying the OER-dominated current onset. In addition, the 2D-assembled architecture may provide more open interfacial pathways for electrolyte contact and product release at high anodic potentials, where EOP becomes more competitive with OER. Therefore, the later onset potential, higher current response in the high-potential region, smaller Tafel slope, and improved ozone generation collectively suggest that the 2D lead oxide/SiO_2 structure favors EOP over OER. Nevertheless, the detailed mechanistic origin, including possible surface reconstruction and lattice-oxygen participation under EOP conditions, requires further operando spectroscopic and theoretical investigations.

Conclusions

We established a molecular precursor-based bottom-up route to synthesize a family of 2D lead glycolates and demonstrated their 2D morphology-preserving conversion to lead oxides. By tuning hydrolysis–condensation kinetics via ethylene glycol coordination with various Pb-EG precursor/water and water/alcohol ratios, we selectively obtained 2D-assembled nanoparticles, 2D-elongated nanostructures, and single-crystalline 2D hexagonal nanoplates. Introducing a SiO_2 overlayer before calcination preserved the 2D architectures during conversion to tetragonal Pb_3O_4, thereby suppressing aggregation and yielding well-defined 2D-assembled Pb_3O_4/SiO_2 with enhanced electrocatalytic performances for EOP. This provides a general strategy for achieving 2D lead oxide materials and a platform for systematic structure–property studies applicable to diverse areas beyond catalysis.

Author contributions

Soohyun Kwon: data curation, formal analysis, investigation, validation, writing – original draft, and writing – review and editing. Woojin Lee: conceptualization, data curation, formal analysis, investigation, validation, writing – original draft, and writing – review and editing. Raquel Aymerich-Armengol: data curation, formal analysis, writing – original draft, and writing – review and editing. Young Mee Jung: formal analysis, resources,

writing – original draft, and writing – review and editing. Seong-Ju Hwang: formal analysis, resources, writing – original draft, and writing – review and editing. Christina Scheu: formal analysis, resources, writing – original draft, and writing – review and editing. Joohyun Lim: conceptualization, data curation, formal analysis, funding acquisition, investigation, methodology, project administration, resources, supervision, visualization, writing – original draft, and writing - review and editing.

Conflicts of interest

There are no conflicts to declare.

Data availability

The data presented in this article are shown as figures. The supporting data have been included in the supplementary information (SI). Supplementary information is available. See DOI:

Acknowledgements

The authors acknowledge the support of the NRF with a grant funded by the Korean government (MSIT) (RS-2024-00345717). This research was supported by the Global Learning & Academic Research Institution for Master's, Ph.D. students, and Postdocs (G-LAMP) Program (RS-2023-00301850) and Basic Science Research Program (RS-2023-00271205) of the NRF grant funded by the Korean Ministry of Education. This research was supported by the International Research & Development Program of the NRF funded by the MSIT (RS-2024-00439825). Synthesis was partly conducted using a high-pressure reactor system at Kangwon National University. Characterization was performed using Quattro S(NFEC-2025-10-308853). This study was supported by 2022 Research Grant from Kangwon National University. This research was supported by the Korean Basic Science Institute (National Research Facilities and Equipment Center) grant funded by the Ministry of Science and ICT (No.RS-2025-00602970).

Notes and references

1. D. Bokov, A. Turki Jalil, S. Chupradit, W. Suksatan, M. Javed Ansari, I. H. Shewael, G. H. Valiev, E. Kianfar, *Adv. Mater. Sci. Eng.*, 2021, **2021**, 5102014.
2. J. Zhao, Y. Liu, M. Fan, L. Yuan, X. Zou, *Inorg. Chem. Front.*, 2015, **2**, 198–212.
3. U. Farooq, T. Ahmad, F. Naaz, S. U. Islam, *Energy & Fuels*, 2023, **37**, 1577–1632.
4. S. Yu, X. Jia, J. Zhang, W. Yang, H. Song, *Chem. Eng. J.*, 2025, **505**, 159639.
5. X. Jiang, Y. Wang, T. Herricks, Y. Xia, *J. Mater. Chem.*, 2004, **14**, 695–703.
6. I. Y. Kim, Y. K. Jo, J. M. Lee, L. Wang, S.-J. Hwang, *J. Phys. Chem. Lett.*, 2014, **5**, 4149–4161.
7. R. Ma, T. Sasaki, *Adv. Mat.*, 2010, **22**, 5082–5104.
8. H. Fu, G. Liu, H. Bao, L. Zhou, H. Zhang, Q. Zhao, Y. Li, W. Cai, *ACS Appl. Mater. Interfaces*, 2020, **12**, 23330–23339.
9. M. Zeng, Y. Xiao, J. Liu, K. Yang, L. Fu, *Chem. Rev.*, 2018, **118**, 6236–6296.
10. L. Zhang, F. Guo, X. Liu, J. Cui, Y. Qian, *J. Cryst. Growth*, 2005, **280**, 575–580.
11. S. Sawatani, S. Ogawa, T. Yoshida, H. Minoura, *Adv. Funct. Mater.*, 2005, **15**, 297–301.
12. S. Shakya, G. V. Prakash, *RSC Adv.*, 2015, **5**, 27946–27952.
13. D. Wang, X. Kan, C. Wu, X. Lin, H. Zheng, K. Li, J. Zhao, Y. Zhao, *Inorg. Chem. Front.*, 2019, **6**, 498–503.
14. A. Bratovcic, in *Lead Chemistry*, ed. P. Chooto, IntechOpen, Rijeka, 2020, DOI: 10.5772/intechopen.91362.
15. J. Liu, X. Peng, X. Wang, X. Zhong, J. Wang, *EES Catalysis*, 2025, **3**, 170–204.
16. Q. Yu, X. Hu, *ChemElectroChem*, 2022, **9**, e202200919.
17. W. Jiang, S. Wang, J. Liu, H. Zheng, Y. Gu, W. Li, H. Shi, S. Li, X. Zhong, J. Wang, *J. Mater. Chem. A*, 2021, **9**, 9010–9017.
18. X. Wang, D. Wu, H. Ge, L. Wang, X. Wu, J. *Environ. Chem. Eng.*, 2023, **11**, 110248.
19. X. Wang, D. Wu, L. Wang, X. Wu, *J. Electrochem. Soc.*, 2022, **169**, 106503.
20. J. Liu, C. Qiu, Z. Xu, M. Xue, J. Cai, H. Shi, L. Ding, X. Li, X. Zhong, J. Wang, *Chem. Eng. J.*, 2023, **468**, 143504.
21. J. Liu, S. Wang, Z. Yang, C. Dai, G. Feng, B. Wu, W. Li, L. Shu, K. Elouarzaki, X. Hu, X. Li, H. Wang, Z. Wang, X. Zhong, Z. J. Xu, J. Wang, *EES Catalysis*, 2023, **1**, 301–311.
22. P. Kumar, J. Liu, P. Ranjan, Y. Hu, S. S. Yamijala, S. K. Pati, J. Irudayaraj, G. J. Cheng, *Small*, 2018, **14**, 1703346.
23. J. Lim, J. Pyo, D. Jung, H.-S. Jung, J.-K. Lee, *J. Sol-Gel Sci. Technol.*, 2016, **79**, 89–97.
24. X. Jiang, T. Herricks, Y. Xia, *Adv. Mat.*, 2003, **15**, 1205–1209.
25. D. Gallagher, T. Ring, *Chimia*, 1989, **43**, 298–304.
26. M. Nogami, Y. Moriya, *J. Non-Cryst. Solids*, 1980, **37**, 191–201.
27. J. Lim, S.-W. Ha, J.-K. Lee, *Bull. Korean Chem. Soc.*, 2012, **33**, 1067–1070.
28. D. L. Green, J. S. Lin, Y. F. Lam, M. Z. C. Hu, D. W. Schaefer, M. T. Harris, *J. Colloid Interface Sci.*, 2003, **266**, 346–358.
29. J. Lim, K. Sim, J.-K. Lee, *CrystEngComm*, 2016, **18**, 2155–2162.
30. N. Tangboriboon, K. Pakdeewanishsukho, A. Jamieson, A. Sirivat, S. Wongkasemjit, *Mater. Chem. Phys.*, 2006, **98**, 138-143.
31. N. Tangboriboon, A. M. Jamieson, A. Sirivat, S. Wongkasemjit, *Appl. Organomet. Chem.*, 2006, **20**, 886-894.
32. T. A. Taha, *J. Mater. Sci.: Mater. Electron.*, 2017, **28**, 12108–12114.
33. Y. Hamed, K. S. Din, S. Harb, S. Elnobi, *Sci. Rep.*, 2025, **15**, 38104.
34. S. Kim, S. Choung, W. Lee, S. Bae, J. W. Han, K. Cho, *J. Mater. Chem. A*, 2022, **10**, 17132–17141.
35. M. Salagram, V. K. Prasad, K. Subrahmanyam, *J. Alloys Compd.*, 2002, **335**, 228-232.
36. E. Ayalew, K. Janssens, K. De Wael, *Anal. Chem.*, 2016, **88**, 1564-1569.
37. C. Zhang, Y. Xu, P. Lu, X. Zhang, F. Xu, J. Shi, *J. Am. Chem. Soc.*, 2017, **139**, 16620–16629.
38. H. Shi, G. Feng, S. Li, J. Liu, X. Yang, Y. Li, Y. Lu, X. Zhong, S. Wang, W. Jianguo, *J. Mater. Chem. A*, 2022, **10**, 5430–5441.
39. H. Shi, X. Wang, X. Peng, M. Xue, Y. Xue, F. Gao, X. Zhong, J. Wang, *J. Mater. Chem. A*, 2024, **12**, 10852–10862.
40. B. Jin, S. Cheng, Y. Sun, P. Xie, L. Li, *Adv. Funct. Mater.*, 2024, **34**, 2314144.

View Article Online
DOI: 10.1039/D6NR00179C

Data availability statements

The data presented in this article are shown as figures. The supporting data have been included in the supplementary information (SI). Supplementary information is available. See DOI: